A Comparative Study on the Electromechanical Properties of 3D-Printed Rigid and Flexible Continuous Wire Polymer Composites for Structural Health Monitoring

Menna A. Saleh[a], Roger Kempers[a], Garrett W. Melenka[a*]

[a] Department of Mechanical Engineering, York University, Toronto, Canada

[*] Corresponding Author: gmelenka@yorku.ca

Abstract

In this study, the electromechanical properties of two different three dimensional (3D) printed continuous wire polymer composite (CWPC) were characterized and compared. The two composite materials are copper wire polylactic acid (PLA) composite (rigid material) and copper wire polyurethane (PU) composite (flexible material). The electromechanical measurements were based on piezoresistive properties of the sensor at which the mechanical strain and the electrical resistance were correlated under uniaxial loading condition. Both types of materials exhibited a direct linear relationship between the two aforementioned quantities indicating the ability of CWPC to be used for real strain sensing applications. The sensitivity, in terms of gauge factor (GF), was compared for the two types of materials. It was found that there is no statistical significance difference between the GF of PLA CWPC (1.36 ±0.14) and PU CWPC (1.29 ±0.07), therefore, the sensing property is depending mainly on the wire integrated in the 3D printed structure rather than the matrix used. Thus, different matrices can be used to fit different applications. An analytical model for GF showed agreement with the experimental results for both materials. As for mechanical properties, PU CWPC showed significant improvement in both Young's modulus (E) and ultimate tensile strength (UTS) by 210.5% and 31.86%, respectively compared to pure PU, while the change in Poisson's ratio (ν) was insignificant. Young's modulus of PLA CWPC was significantly increased by 80.3% compared to PLA, while UTS and ν were not significantly changed. The experimental mechanical properties were statistically compared with analytical models' data and showed good agreement with them. The outcome of this study focused on the manufacturing of 3D printed functionalized structure with improved mechanical properties to be used in wide range of applications based on the range of strain needed such as rigid sports equipment and flexible wearable sensors.

Keywords: Fused filament fabrication, Structural health monitoring, Polylactic acid composite, Polyurethane composite, Electromechanical properties, Mechanical properties

1. Introduction

Polymer-matrix composites (PMC) have drawn growing attention in the past decades due to their strength and light weight. They have been extensively used in industrial fields such as automotive, astronautics, and aeronautics [1]. For such sectors, composites must possess the required mechanical properties while subjected to harsh environmental conditions such as radiation, corrosion, and thermal aging. Accordingly, the manufacturer needs to ensure these properties and users should have an efficient and reliable method to check the part suitability during service. For

real-time and in-situ structural health monitoring (SHM), polymer composites with sensing capabilities are extremely favourable [1,2]. SHM is important for safety issues by continuously monitoring the deformation of the composite under mechanical loading for any internal change, damage or failure and thus increasing the life cycle of the product [3–5].

Different processing techniques have been used to produce conductive polymer composites by incorporating various conductive fillers such as copper, aluminum, graphite, carbon nanotubes, carbon fibers, and graphene. The processing techniques studied in literature are magnetic stirring, template methods, and melt processing [6,7]. Although these methods are cost effective, they can not produce complex geometries in short times with customizable sensing capabilities. Additionally, these methods are not suitable for large-scale production. Additive manufacturing (AM) is introduced as an emerging technology to fabricate complex three-dimensional geometries. Among various AM techniques, extrusion-based is a promising process due to its simplicity and cost-effectiveness. Extrusion-based fabrication is a solid-state AM method called Fused Filament Fabrication (FFF) process that uses polymer filament to fabricate three-dimensional structures [8].

Most research, based on the process of extrusion-based AM, has focused on relatively rigid polymers such as polylactic acid (PLA) and ABS. However, flexible polymers offer a wider range of strains and low elastic modulus, which broaden the scope of sensing applications such as pressure sensors, displays, flexible circuits, wearable sensors, and piezoresistors. The development of flexible sensory composites allows for their use in the next generation technology of Internet of Things (IOT) devices for human-machine interface [2,8]. Despite its advantages, printing parts using flexible filament of rubber-like materials still faces some challenges such as filament buckling. Thus, there is a need to improve a reliable, economically, and simple method to fabricate flexible sensory composites [8].

Flexible polymer used for sensing applications had been investigated by several researchers [2,8–10]. For instance, Bertolini et al. [9] studied the conductivity of carbon black-polypyrrole (CB-PPy) particle reinforced poly(vinylidene fluoride)/thermoplastic polyurethane (PVDF/TPU) 3D printed flexible composite. They compared the effect of FFF and compression molding processes on the conductivity of the composite. Qureshi et al. [11] used a flexible strain sensor in the form of wire made of conductive silver nanoparticles deposited on the surface of nylon yarn. This single wire was further embedded in a glass fiber reinforced resin composite for resistance measurements under flexural loading. Yet, 3D printed continuous wire reinforced flexible polymer composite has not been explored for sensing applications where the wire is integrated in the part to also enhance its mechanical properties.

For sensing applications, there are different mechanisms for electromechanical strain sensing such as capacitance, piezoresistance, and inductance. Strain sensors based on capacitance and inductance have limited responsive capabilities to vibrations and are difficult to mount to the structure for commercial applications. They also require complex integrated circuits. In contrast, piezoresistive based strain sensors commercially available of metallic materials are highly functional in sensing applications [10]. In the piezoresistive method, change is resistance ($\Delta R/R$) is measured to calculate the resultant strain (ε) from the equation of gauge factor (GF) which is a property of a material as shown in Equation 1 [5].

$$GF=(\Delta R/R)/\varepsilon \quad (1)$$

where ΔR is the difference between the initial resistance of sample before loading (R) and the instantaneous measured resistance of the sample during loading.

Saleh et al. [12] studied the applicability of additively manufactured continuous wire PLA composites using two types of wires for SHM. The gauge factor was found to be 1.17 ±0.06 and 1.13 ±0.07 for copper and nichrome wire PLA composites, respectively. Continuous wire not only used for sensing by resistance measurements, but it also increased the mechanical properties of the composite. However, functional composite of continuous wire with flexible polymer has not been investigated for SHM.

Resistance response to stretching could be recorded in one or two directions depending on the structure of the sensor used [13]. Due to the complex nature and heterogeneity failure modes of the fiber-reinforced composite, full characterization of composites failure is required through non-contact strain measurement. This can be done by measurement of both axial and transverse to fully understand the mechanical behaviour of the composite. The method used is called two-dimensional digital image correlation (2D-DIC) [14]. DIC has been commonly used to detect surface deformation of composites. It is a powerful tool that offers flexibility in surface measurements for solid mechanics. 2D DIC compares collected digital images of specimen surface before and after deformation to obtain full-field displacements and strains [15,16].

In this study, a comparison between the electromechanical behavior of rigid PLA-based material and hyperelastic polyurethane (PU)-based material is investigated to understand their performance for SHM applications. Here, the FFF technique was applied to fabricate the samples at which the metal wire is integrated within the 3D structure of polymer composites to act as strain sensor. Two matrices (PLA and PU) were used and the functionality of continuous wire polymer composite (CWPC) was examined based on the GF values. To obtain the full field strain of the sample under tensile loading, the 2D DIC technique was applied. Rule of mixture (ROM) and hyperelastic analytical models were introduced to compare the experimental mechanical properties with the theoretical calculated values. An analytical model for electromechanical properties was proposed to verify the results of the GF for both PLA and PU CWPCs.

2. Experimental methods

2.1. Materials

Two polymer matrices were used which are PLA filament (1.75 mm Transparent PLA, ColorFabb, The Netherlands) and flexible PU filament (1.75 mm Transparent PU, Ninjatek, USA). The electrically conductive element was a polyimide coated copper wire was used (75 µm Cu wire, Remington Industries, USA) to serve as the integrated health monitoring sensor.

2.2. Sample fabrication

An open-source 3D printer (Prusa i3 mk2, Prusa Research, Prague, Czech Republic) was modified to fabricate the CWPC samples. The 3D printer was modified, and the samples were fabricated using the method detailed by Ibrahim et al. [17]. CWPC samples were manufactured following the ASTM D3039 -17, 2017 with dimensions of 200 mm x 25 mm x 2 mm. To print the composites

samples, G-code was generated using a customized MATLAB code (MATLAB R2019b, Natick, Massachusetts: The MathWorks Inc.). G-code was used to define the axes movements to print the samples in a axial parallel pattern which was not available in the commercial slicing software. Table 1. Printing parameters of CWPC samples.Table 1 presents the printing parameters used to prepare the samples. Extruder temperature and bed temperature were selected based on the recommendation of materials manufacturers. Nozzle diameter was selected to accommodate composite printing with wire. Other geometrical parameters were chosen according to the ASTM standard as mentioned before. For example, the raster parameters were selected to form the two-dimensional surface area of the sample (single layer) through the nozzle movement in both x and y axes. Then the nozzle is moved upward in z direction by the layer thickness to form the second layer and so on till the thickness of the sample is achieved. Figure 1 shows a 3D printed sample with principle axes. Four configurations were printed which are pure PLA, Cu wire reinforced PLA (PLA+Cu), pure PU, and Cu wire reinforced PU (PU+Cu).

Table 1. Printing parameters of CWPC samples.

	Material Type		Unit
	PLA, PLA+Cu	PU, PU+Cu	
Extruder temperature	200	220	°C
Bed Temperature	50	55	°C
Nozzle diameter	1		mm
Wire diameter	0.075		mm
Raster width	0.65		mm
Layer height	0.5		mm
Printing angle	0		°
Number of rasters	38		
Number of layers	4		
Fill density	100		%

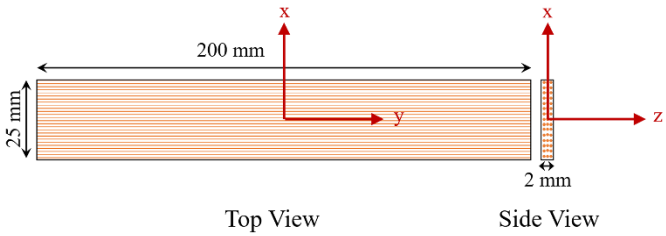

Figure 1. 3D printed sample with principle axes.

Samples were prepared for electrical measurements following the method presented by Saleh *et al.* [12]. PLA end tabs were printed and used to avoid slippage between the sample and the test

frame grips to ensure that the sample fails within the gauge length. End tabs have rectangular shape with dimensions of 60 mm x 25 mm x 2 mm and a taper angle of 6.7°. The sample with bonded end tabs was prepared as in [12]. Four samples of each CWPC configuration were prepared.

2.3. Electromechanical testing

The sample were electromechanically characterized by measuring the electrical resistance of the embedded copper wire under tensile loading. The electrical resistance was recorded using in-situ digital multimeter (DMM) (Agilent 34401A, Agilent Technologies, Incorporated, Colorado, USA). To eliminate lead wire resistance, four-probe method was applied. Customized MATLAB script was used to acquire the data at frequency of 1 Hz. The sample was loaded with constant crosshead speed of 2 mm/min using dynamic test frame (Instron ElectroPlus Model E3000, Norwood, USA) equipped with 3 kN load cell. The load and displacement were acquired using data acquisition (DAQ) (DAQ M Series, NI USB-6210, National Instrument, Texas, USA). The data acquired with the DAQ is synchronized with the DMM using MATLAB script at the same frequency rate of 1 Hz. The sample extension was measured using 2D DIC system which is also synchronized with the DAQ and DMM in the same MATLAB script. Figure 2 shows the experimental setup of this study.

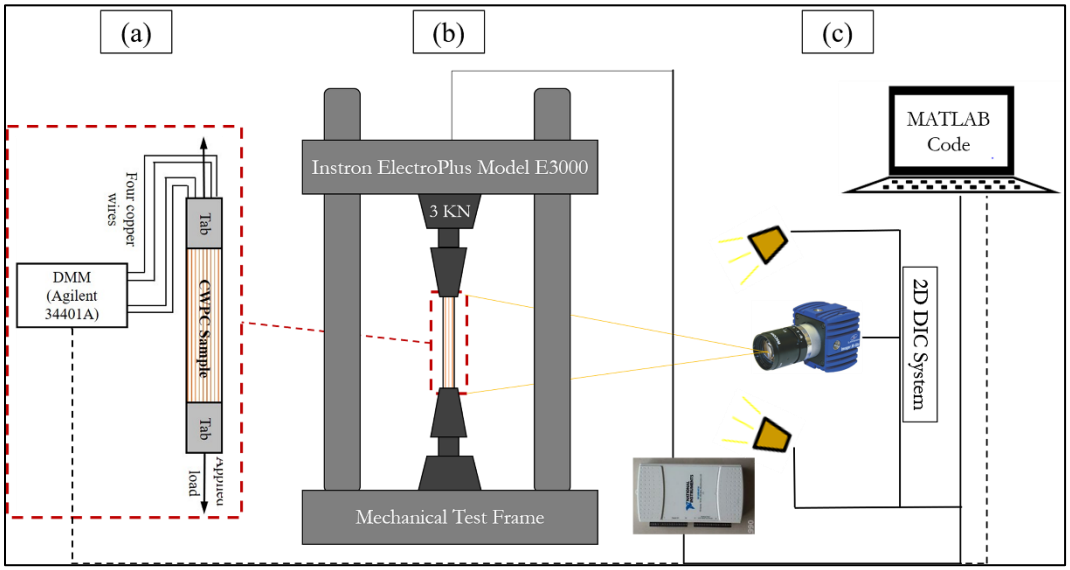

Figure 2. Experimental setup of electromechanical testing. (a) test sample with integrated sensor (b) electrodynamic test frame for quasi-static and dynamic evaluation of the sensor (c) 2D DIC system for full field strain measurement.

A 5M Basler camera (acA2440-35um, Basler AG, Germany) placed 0.5 m away from the sample was used to acquire the images at a rate of 1 Hz with area of interest (AOI) on the sample of (60 mm x 70 mm) as shown in **Error! Reference source not found.**. 50 mm focal length lens (KOWA LM50JCM 2/3" 50MM F2.8, RMA electronics, USA) was employed and two light emitted diode (LED) panels (Neewer 2 Packs LED light, China) were used to illuminate the sample.

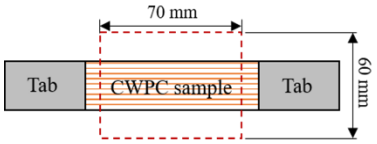

Figure 3. AOI on the CWPC sample.

The digital image correlationsoftware package (DaVis version 10.0.3 StrainMaster, LaVision GmbH, Gottingen, Germany) was used to conduct the strain measurements for the acquired images. First, samples were painted black using (2X Ultra Cover, Rust-Oleum Corp, Concord, ON) and white speckled with a mixture of white paint (5211 Opaque White, Createx Airbrush Colors, Createx Colors, East Granby, CT) and reducer (4012 High Performance Reducer, Createx) to achieve high contrast of speckle pattern for the process of image correlation. An airbrush (H-SET, Paasche Airbrush Company, Chicago, IL) was used to apply the speckling pattern. An example of speckled sample is shown in Figure 4 along with a profile of grayscale count across the width of the sample. Figure 4 (b) shows the alternation between the peaks and valleys across the width representing the alternation between black and white colors and hence a good contrast for the image. Second, the images were divided into 49 x 49 pixels subsets size with 16 pixels step size such that each subset has an average of 5 speckles to be used in image post processing. Each subset was correlated with another subset in the consecutive image following least squares displacement measurements algorithm to get the displacement vector. Partial derivative of the displacement vector field was calculated to compute the strain occurring between two consecutive images. Calculated average value of strain within each field of view (25 mm x 50 mm) was finally plotted against the corresponding tensile stress to obtain the stress-strain curve of each sample. This curve is used to obtain the ultimate tensile strength (UTS) and Young's modulus (E) of each sample. From 2D DIC images, both axial and transverse strains were calculated to obtain Poisson's ratio (Equation 2).

$$\nu = -\frac{\text{lateral strain}}{\text{axial strain}} \tag{2}$$

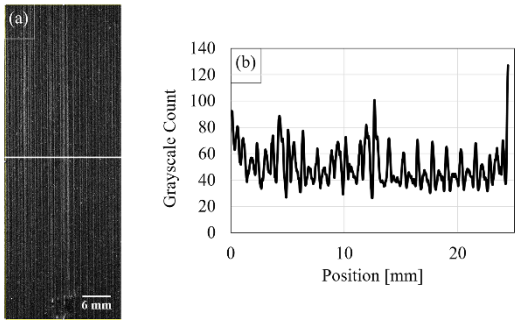

Figure 4. a) Example of 3D printed speckled sample; b) A profile of grayscale contrast of the speckled pattern extracted at the middle of the sample (indicated by horizontal white line in part a).

The wire sensors sensitivity was determined based on the GF calculation as shown in Equation 1. The GF value is based on the fractional change of electrical resistance (Equation 3) [18] and the ε_{yy} strain calculated from 2D DIC system.

$$\text{Fractional change of electrical resistance } (\Delta R/R) = \frac{R_i - R}{R} \quad (3)$$

where R_i is the measured resistance of the sample during loading and R is the initial resistance of sample before loading.

3. Analytical modelling

To verify the experimental data of mechanical properties and since the two types of materials are different with respect to their stiffness, different analytical models must be selected to fit each type. Rule of mixture (ROM) model assumes rigid material with continuous reinforcement; therefore it was chosen to study the properties of PLA CWPC. Since PU CWPC is flexible, so analytical model for hyperelastic materials were chosen to study it.

3.1. Rule of Mixture (ROM) model

For the continuous wire reinforced PLA composite, rule of mixture (ROM) was used to predict its mechanical properties [17,19]. Equations 4 were used to predict the UTS, Young's modulus, and Poisson's ratio. Individual properties and volume fraction of each constituent need to be identified. Table 2 lists the Cu wire assumed properties of UTS, Young's modulus, and Poisson's ratio [17]. While PLA UTS, Young's modulus, and Poisson's ratio were experimentally determined (as mentioned in sec. (2.3)) for the printed polymer and these experimental values will be listed later in sec. (4.2).

$$\sigma_c = V_w\sigma_w + V_p\sigma_p \quad (4\text{-a})$$

$$E_c = V_wE_w + V_pE_p \quad (4\text{-b})$$

$$\nu_c = V_w\nu_w + V_p\nu_p \quad (4\text{-c})$$

where σ_c, σ_w, and σ_p are the UTS of composite, wire, and polymer, respectively. E_c, E_w, and E_p are Young's modulus of composite, wire, and polymer, respectively. ν_c, ν_w, and ν_p are Poisson's ratio of composite, wire, and polymer, respectively. V_w and V_p are the volume fractions for both wire and polymer, respectively. V_w and V_p were mathematically calculated following the method mentioned in [12].

Table 2. Mechanical properties of Cu wire [17].

Material	Material Properties		
	Young's modulus (GPa)	UTS (MPa)	Poisson's ratio
Cu wire	110	210	0.355

It is common for 3D printed parts to include voids. Thus the ROM in terms of matrix property was modified to account for them as reported by several researchers [13,20,21].

3.2. Hyperelastic analytical model

According to literature [22], three classifications of hyperplastic models were formulated depending on the development of the model function. The first model is driven based on a

mathematical development of energy strain function, the second model is based on conducting experimental data (empirical model), and the third model is based on physical motivation such as polymer chains network physics and statistical methods. Each of these formulations were used in this study to anticipate the hyperelastic mechanical behaviour of PU CWPC. Mooney-Rivlin two parameters model represents the model developed using the strain-energy function, the Yeoh model is based on experimental findings, and Neo-Hookean model utilizes network physics and statistical methods. In these models, the sample is transversely isotropic as its cross-section plane is plane of isotropy where the properties are the same in all directions and it was also assumed to be incompressible under uniaxial tensile load such that Equations 5 and 6 are valid [23].

$$\lambda_1\lambda_2\lambda_3 = 1 \tag{5}$$

$$\lambda_1 = \lambda, \qquad \lambda_2 = \lambda_3 = \frac{1}{\sqrt{\lambda}} \tag{6}$$

where λ is the stretch ratio along the principal axes (λ = 1 + strain).

The formulas to predict the three hyperelastic analytical models are presented in Equations 7-9 [23];

Neo-Hookean model: $\sigma_{Hookean} = 2(\lambda^2 - \frac{1}{\lambda})C_1$ (7)

Mooney-Rivlin two parameters model: $\sigma_{Mooney} = 2(\lambda^2 - \frac{1}{\lambda})(C_1 + C_2\frac{1}{\lambda})$ (8)

Yeoh model: $\sigma_{Yeoh} = 2\left(\lambda^2 - \frac{1}{\lambda}\right)(C_1 + 2C_2\left(\lambda^2 + \frac{2}{\lambda} - 3\right) + 3C_3\left(\lambda^2 + \frac{2}{\lambda} - 3\right)^2)$ (9)

where $\sigma_{Hookean}$, σ_{Mooney}, and σ_{Yeoh} are applied stresses in a uniaxial direction, and C_1, C_2, and C_3 are material parameters.

To obtain material parameters of these analytical models, curve fitting of experimental data of stress-stretch curve was applied through least-square and Levenberg-Marquardt type algorithm methods by Comsol software (Comsol Multiphysics 5.5, Stockholm, Sweden). In this software, the optimization tool of aforementioned algorithm was used to build the model. For this model, the parameters in terms of material parameters and stretch were defined and the equation was defined in terms of stress.

Then, the obtained material parameters were used to plot stress-strain curve for each analytical model. Finally, the obtained stress-strain curve was used to produce the theoretical UTS and Young's modulus for each sample and then compare these values with the experimental ones.

To test the efficiency of the analytical model, Equation 10 was applied to calculate the relative error between the optimal numerical fitting and the experimental data [24];

$$Error = \frac{\sigma(\lambda_i, parameters) - \sigma_{exp_i}}{\max\{0.5|\sigma_{exp_i}\}} \qquad i = 1, \dots, m \tag{10}$$

where $\sigma(\lambda, parameters)$ is the analytical model stress function, σ_{exp} is the experimental tensile stress, and m is the number of readings. There is a slight modification in the denominator, as

reported by [24], where 0.5 is included to avoid the division by a small value of σ_{exp} when λ approaches 1. The average error was finally calculated to assess the difference between theoretical and experimental results [24].

3.3. Gauge factor model

Theoretical values of gauge factor of PLA and PU CWPCs were predicted using an analytical model as described in [12]. In this model, the change in resistance is calculated corresponding to each mechanical strain using Equation 11. In this equation, when the structure is subjected to mechanical strain, the corresponding resistance (R) is varies due to the geometrical changes of the conductive constituent in the composite in terms of cross-sectional area reduction and elongation.

$$R_i = \frac{\rho L_i}{A_i} \tag{11}$$

where L_i, A_i, and R_i are instantaneous values of the wire length, area, and electrical resistance, respectively, corresponding to the applied strain. ρ is the resistivity of the copper wire.

The experimental strain data was plotted against the calculated change in resistance ($\frac{R_i - R}{R}$) and the slope of this curve was used to obtain the theoretical GF value as indicated in Equation 1.

Analytical and experimental GF values were compared for statistical significance using a paired sample T-test with an accepted confidence level of 95% ($p < 0.05$).

3.4. Microscopic imaging

The samples were cut to examine the cross-section and quantify the wire volume fraction within the printed part using an optical microscope. A clear resin (Amazing clear cast, Alumilite Corp, USA) was used to mount the samples in a mold of 28 mm inner diameter, then cured for 24 hours. A high-speed cutting cut-off saw (Mecatome T260, PRESI, Hungary) was used to section the samples. Then sample surface preparation was carried out on a grinding and polishing machine (StarGrind™ 200-2V, Microstar 2000, Canada) at a rotational speed of 300 rpm. Silicon carbide papers with a sequence of 180, 280, 400, and 600 grit were used followed by polishing using a suspension of 1 μm alumina particles. Optical Stereomicroscope (LEICA MZ10 F, LEICA, Germany) was used at 50x magnification to quantify the volume fraction of printed polymer composite constituents. Finally, open-source image processing software (ImageJ, National Institutes of Health, Bethesda, Maryland, USA) was used to process captured images and calculate the volume fraction.

4. Results and discussion

4.1. Optical microscopy

Figure 5 presents the cross-section of PLA and PU CWPCs 3D printed samples. It can be noted that the wire is uniformly distributed within the sample for the both cases of PLA and PU CWPCs. The voids were found mainly around the wire. To calculate the volume fraction of each constituent of the fabricated composite, ImageJ software was used to process the optical microscope images (Figure 5 (a, b)). Threshold tool was applied to identify voids within the sample and to compute the void volume fraction (V_v%) (Figure 5 (c, d)), then, similarly, the volume fraction of the wire

(V_w%) was calculated (Figure 5 (e, f)). Table 3Table 1 summarizes the volume fraction values of each constituent. It can be noticed that the V_v% for PU CWPC is less than that of PLA CWPC and this may be attributed to the more flexibility of PU matrix compared to PLA.

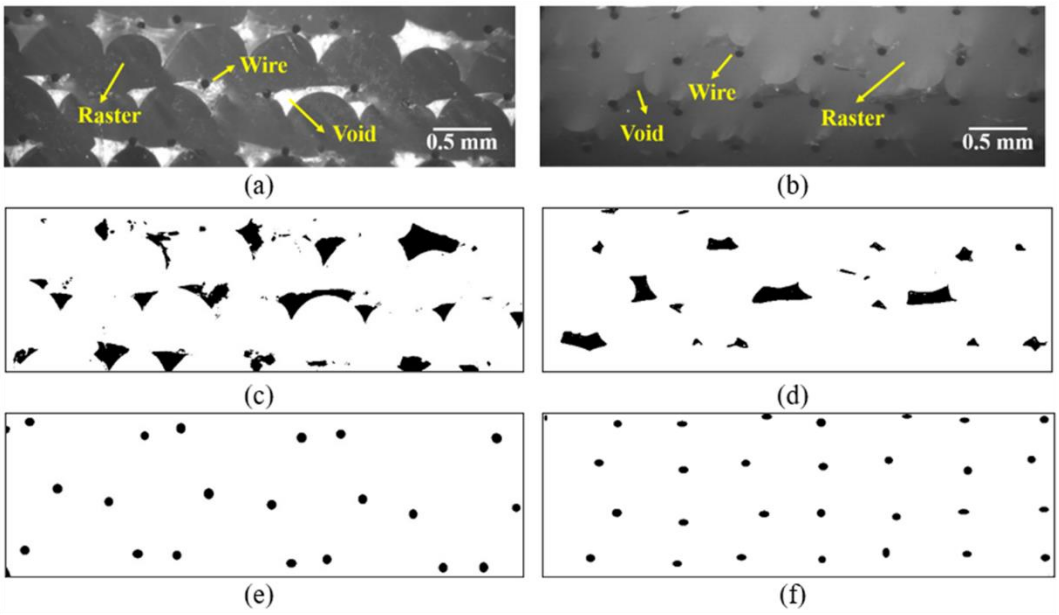

Figure 5. Microscopy cross-section of; a) PLA+Cu, b) PU+Cu. Processed images to calculate V_v% of; c) PLA+Cu, d) PU+Cu. Processed images to calculate V_w% of; e) PLA+Cu, f) PU+Cu.

Table 3. Volume fraction of PLA and PU CWPCs constituent.

	Cu wire reinforced PLA composite	Cu wire reinforced PU composite
Matrix (V_p%)	91.9 (±0.76)	94.05 (±0.83)
Wire (V_w%)	1.8 (±0.006)	1.7 (±0.007)
Void (V_v%)	6.3 (±0.017)	4.25 (±0.014)

4.2. Mechanical properties

Full filed strain distributions measured using 2D DIC system in axial and transverse directions are presented in Figure 6 and Figure 7 for both PLA CWPC and PU CWPC. Higher flexibility of PU compared to PLA can be clearly observed in these figures (Figure 6 and Figure 7). Figure 6 shows axial full field strain distribution at different stress levels. It can be noted that the PU CWPC shows higher positive axial deformation from the start of the test until just before the failure of the sample compared to PLA CWPC under tensile loading. For the transverse direction, as shown in Figure 7, it can also be seen that the PU CWPC can sustain more deformation compared to PLA CWPC throughout the tensile test following the same trend of the deformation in the axial direction.

As mentioned in Section. 2.3, 2D DIC results were used to calculate the average strain for each image and then plot it against the corresponding tensile stress to obtain the stress-strain curve of each type of material. Figure 8 shows stress-strain curves for PLA and PU CWPCs. This figure

verifies the DIC results as it can be noted that PU CWPC samples sustain failure strain six times larger than that of PLA CWPC samples. While, PLA CWPC has higher strength compared to PU CWPC.

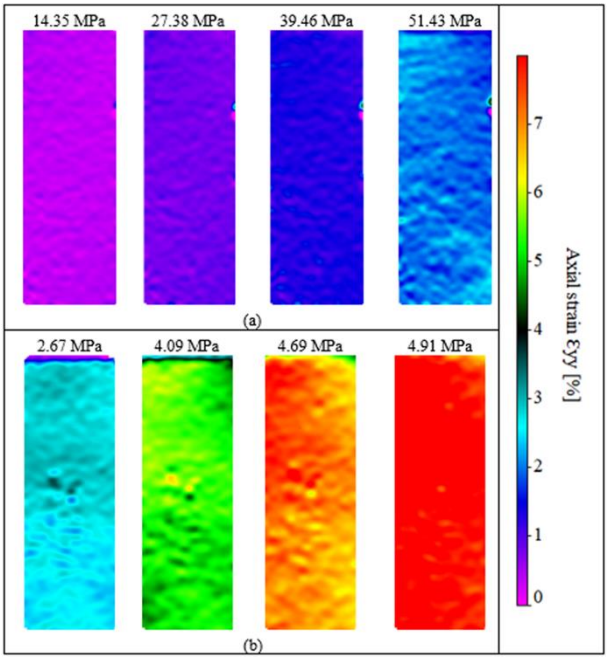

Figure 6. The progression of axial strain obtained using 2D DIC strain measurement just before failure of; a) PLA CWPC, b) PU CWPC.

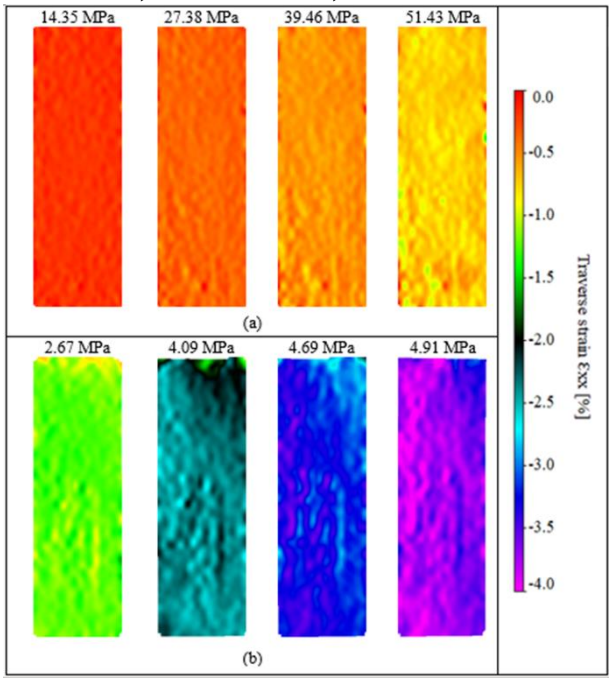

Figure 7. The progression of transverse strain obtained using 2D DIC strain measurement just before failure of; a) PLA CWPC, b) PU CWPC.

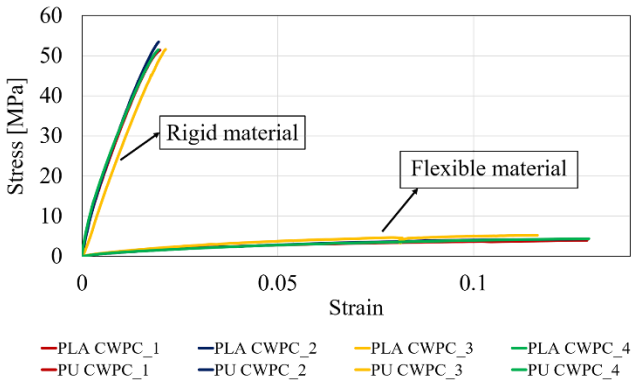

Figure 8. Example of stress-strain curve for PLA and PU CWPCs.

To demonstrate the difference of the full field strain between each type of material under tensile loading, 2D DIC results were compared for both PLA and PU CWPCs at the same stress level. Figure 9 shows the full field strain distribution at 2 MPa stress level. It can be noted that both axial and transverse strain are higher in case of PU CWPC compared to PLA CWPC. PLA CWPC almost did not experience any strain at this small stress level for both axial and transverse direction, while PU CWPC strained by about 2% and -1% for axial and transverse direction, respectively.

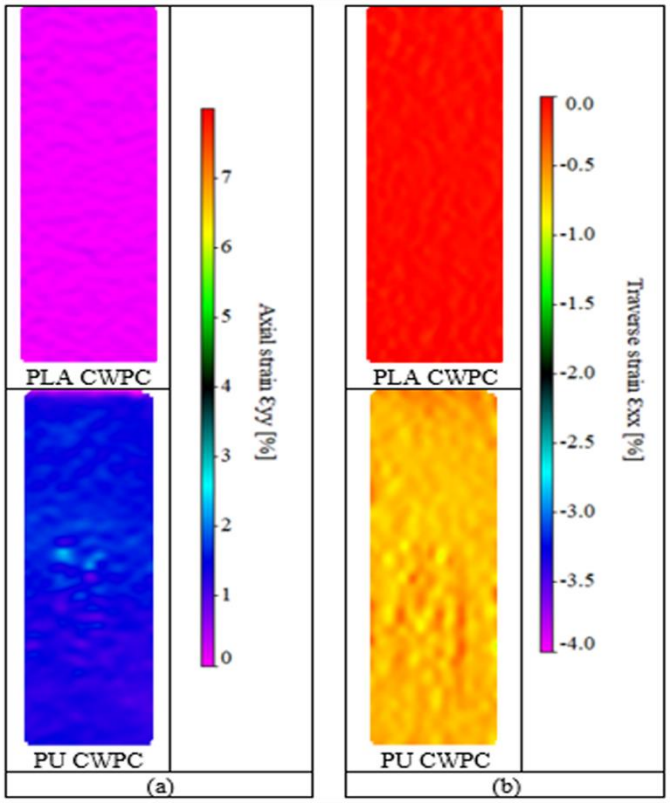

Figure 9. Full field strain distribution at stress level of 2 MPa for PLA and PU CWPCs; a) axial strain ε_{yy}, b) transverse strain ε_{xx}.

Error! Reference source not found. compares the experimentally obtained mechanical properties (ultimate tensile strength (UTS), Young's modulus (E), and Poisson's ratio (ν)) of PLA, PLA+Cu,

PU, and PU+Cu. It can be shown that both UTS and Young's modulus of PLA based materials are larger than that of PU based materials. While ν is larger for PU based materials and this is because the higher flexibility of PU compared to PLA. Young's modulus was improved by 80.3% and 210.5% for PLA composite and PU composite, respectively compared to pure PLA and PU. From the statistical analysis comparing the pure materials with the composite ones, it is shown that UTS was significantly improved only for the case of PU based materials by 31.86% and this may be attributed to the larger difference in UTS between PU and Cu compared to PLA based materials. While, Young's modulus was found to be significantly improved for both PLA CWPC and PU CWPC compared to PLA and PU, respectively. Poisson's ratio was not significantly changed for composite materials compared to pure ones. These statistical results are presented in Table 4 through applying independent sample t-test with confidence level of 95%.

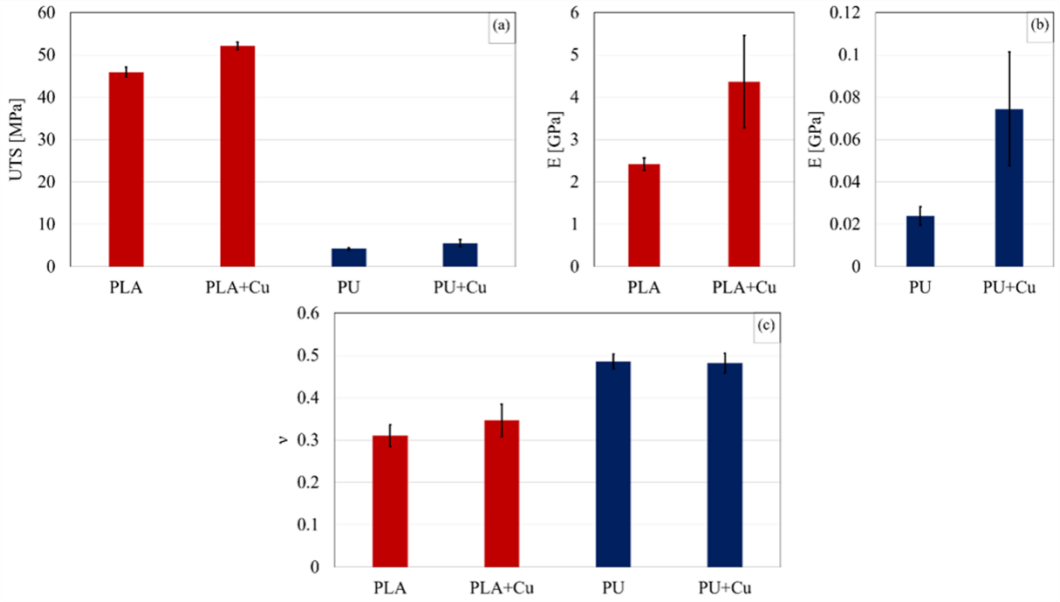

Figure 10. PLA, PLa+Cu, PU, and PU+Cu mechanical properties; a) Ultimate tensile strength (UTS), b) Young's modulus (E), and c) Poisson's ratio (ν).

Table 4. Independent sample t-test to compare mechanical properties of PLA with PLA+Cu and PU with PU+Cu (S: statistically significant, NS: statistically not significant).

		P-value	Significance
Ultimate Tensile Strength (UTS)	PLA & PLA+Cu	0.889	NS
	PU & PU+Cu	0.019	S
Young's Modulus (E)	PLA & PLA+Cu	0.044	S
	PU & PU+Cu	0.015	S
Poisson's Ratio (ν)	PLA & PLA+Cu	0.128	NS
	PU & PU+Cu	0.775	NS

4.3. Mechanical model results

To verify the experimental data, analytical models for mechanical properties of rigid and hyperelastic materials were applied as indicated in Sections. 3.1 and 3.2. For hyperelastic analytical models, Figure 11 presents an example of stress strain curve of PU CWPC sample comparing the experimental data and the three different applied hyperelastic analytical models. It can be noted that the Neo-Hookean analytical model has the largest error (calculated using Equation 10) compared to the experimental results as confirmed by the error bar chart showed in Figure 12. In this figure, both Mooney-Rivlin 2 parameters and Yeoh analytical models have a small error of 0.066 ± 0.006 and 0.095 ± 0.027, respectively, with respect to the experimental data and since Mooney-Rivlin is easier to implement than Yeoh analytical model, it was chosen for further analysis.

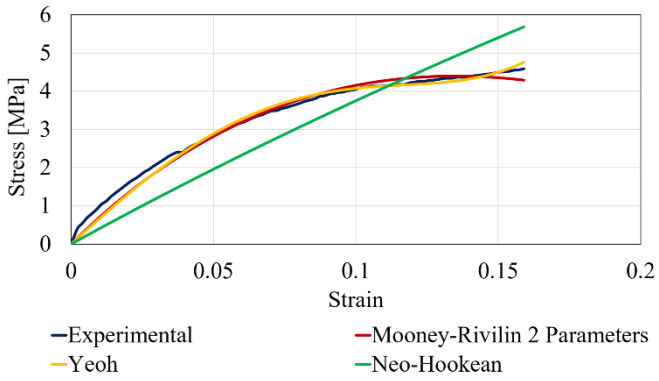

Figure 11. Example of experimental and hyperelastic analytical models for PU CWPC.

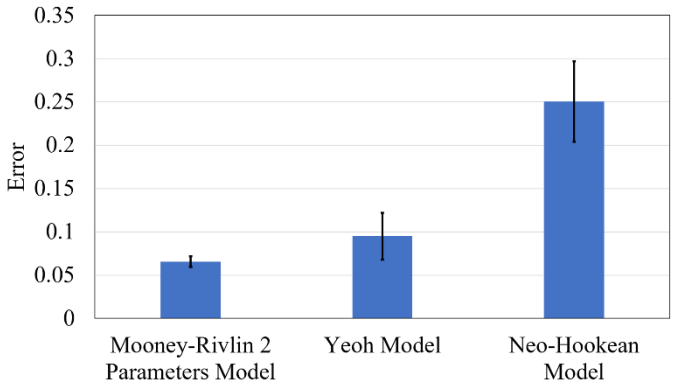

Figure 12. Average error between hyperelastic analytical models and experimental data for PU CWPCs.

The difference between experimental and theoretical values may be attributed to the lack consideration of the analytical models of the fiber matrix interaction. For PLA CWPC, ROM was applied as mentioned in Section. 3.1 using V_w to be 1.448% and V_p to be 98.552%. **Error! Reference source not found.** shows the experimental values of UTS, Young's modulus, Poisson's ratio versus the analytical model values of the same properties for PLA and PU CWPCs. There is a slight difference between the experimental and the analytical model data which may be attributed to the simple assumption of the model without taking into consideration the complexity of the fabrication process and damage mechanism as reported by [25].

To confirm the credibility of these models, paired sample t-test with confidence level of 95% was applied and the results for both ROM model and Mooney-Rivlin model versus the experimental data are presented in Table 5. The statistical analysis showed a good agreement between the experimental and analytical model data since there is no statistical significance difference between them according to the p-value.

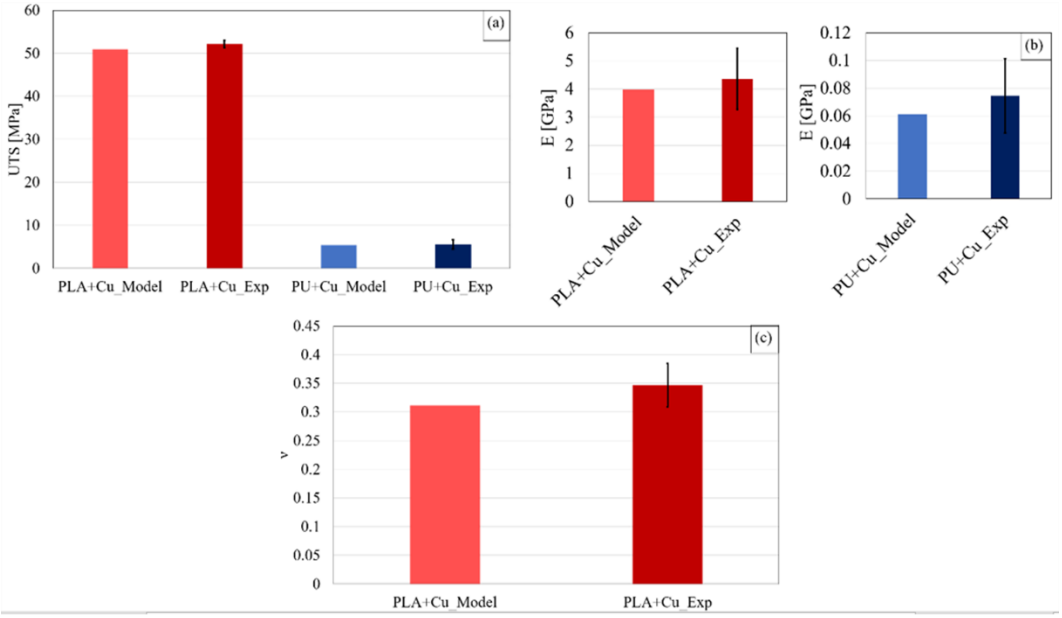

Figure 13. Experimental and analytical results of mechanical properties of PLA and PU CWPCs; a) UTS, b) Young's modulus, and c) Poisson's ratio.

Table 5. Paired sample t-test of theoretical and experimental mechanical properties (NS: statistically not significance).

		P-value	Significance
Ultimate Tensile Strength UTS (Model vs. Exp)	PLA+Cu	0.054	NS
	PU+Cu	0.052	NS
Young's Modulus E (Model vs. Exp)	PLA+Cu	0.527	NS
	PU+Cu	0.09	NS
Poission's Ratio ν (Model vs. Exp)	PLA+Cu	0.158	NS
	PU+Cu	N/A	N/A

4.4. Electromechanical properties

Figure 14 shows an example of the relative change of electrical resistance under tensile strain for both PLA and PU CWPCs. The direct linear relationship between the change in resistance and strain proves the ability of this materials to be used as strain sensor. This agrees with previous obtained results [12]. The sudden increase in the value of the change of electrical resistance

indicates a failure of wire and loss of conductivity, therefore, this sensor can not only be used to predict the deformation, but also it can be used to indicate the failure mechanism. To obtain the GF, the slope of the first linear part of the graphs in Figure 14 was calculated. The sensitivity of composites using Cu wire in terms of GF were found to be about 1.36 ±0.14 and 1.29 ±0.07 for PLA and PU CWPCs, respectively as shown in Figure 15. An independent sample t-test ($p = 0.05$) was performed to compare the GF of PLA and PU CWPC samples and it was determined that statistical difference was not detected (Table 6). This indicates the sensor depends on the wire only regardless of the matrix used. However, the PU CWPCs sustained more strain before breakage of the wire compared to PLA CWPCs as depicted by stress-strain curves for PLA+Cu and PU+Cu sample (Figure 8). The higher strain before failure of the PU CWPCs is due to its lower stiffness as shown in **Error! Reference source not found.**-b. Therefore, different types of matrices can be used to fit different applications such as rigid sports equipment and flexible wearable sensor.

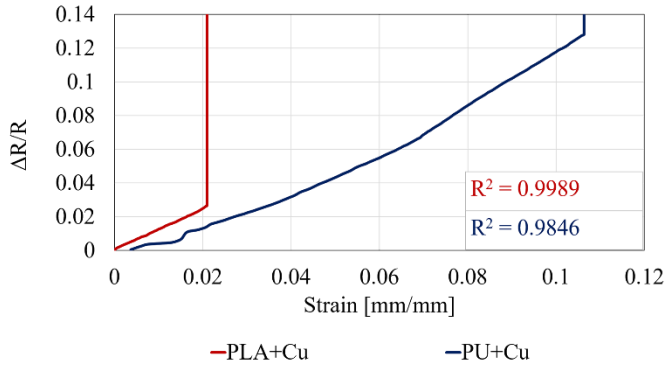

Figure 14. Plot of (ΔR/R-strain) curve

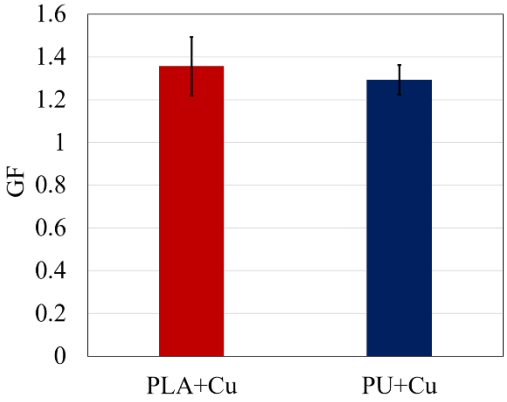

Figure 15. GF of PLA and PU CWPCs.

Table 6. Independent sample t-test for GF (NS: statistically not significance).

		P-value	Significance
GF	PLA+Cu & PU+Cu	0.456	NS

The sensitivity of both composites was compared with the analytical model as explained in Section. 3.3 (Figure 16). As shown in Figure 16, there is a small standard deviation for the theoretical GF bars because the electrical resistance was calculated based on an the change of experimental tensile extension as indicated by Equation 3 and 11. Paired sample t-test with confidence level 95% was applied to statistically analyze the significance between the theoretical and experimental GF of PLA and PU CWPCs. Table 7 approves the credibility of this analytical model to be used to predict the GF as there is no significance difference between theoretical and experimental data.

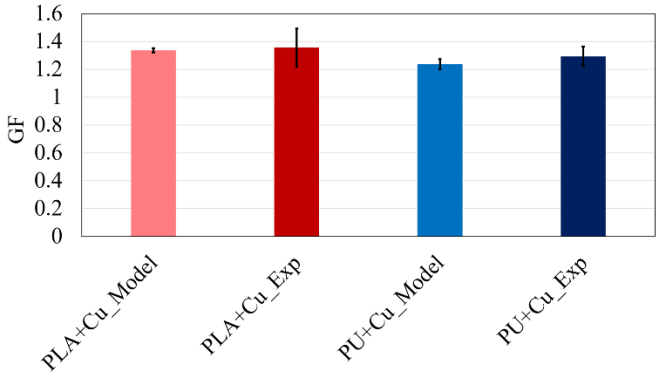

Figure 16. Comparison of experimental and analytical model GF for PLA and PU CWPCs.

Table 7. Paired sample t-test of theoretical and experimental GF (NS: statistically not significance).

		P-value	Significance
GF (Model vs. Exp)	PLA+Cu	0.772	NS
	PU+Cu	0.342	NS

5. Conclusion

The two types of polymer matrix composites of rigid and flexible matrices with integrated continuous copper wire were successfully compared in terms of their electromechanical properties to be used for structural health monitoring applications. This verify the 3D printing capabilities to fabricate sensors with tunable properties. For instance, the 3D printing PLA CWPC can be used for rigid applications such as sporting equipment while the PU CWPC can be used for flexible ones such as wearable sensors.

Direct relationship between the strain and the change in resistance for PLA and PU CWPCs indicates the applicability of these 3D printed structure to be used as strain sensor. The electromechanical properties of both composites showed the dependency of the strain sensor on the integrated wire regardless the type of matrix used as the GFs of 1.36 ±0.14 and 1.29 ±0.07 for both PLA CWPC and PU CWPC, respectively, are statistically insignificant. Therefore, different matrices can be used to fit different applications encompassing wider range of strains. Analytical model based on electrical resistance equation to get the GF showed agreement with the experimental measured GF for both PLA and PU CWPCs.

Mechanical strain was calculated using 2D-DIC technique to obtain full field strain and to be able to calculate Poisson's ratio. DIC images of both axial and transverse strains showed higher flexibility of PU CWPC compared to PLA CWPC by comparing the values of strain for both composites at the same stress level (2 MPa). The stress-strain curve for both type of composites (PLA and PU CWPCs) showed a higher flexibility of PU compared to PLA as the PU CWPC strain was around six times higher than the PLA CWPC. Ultimate tensile strength (UTS) and Young's modulus ϵ were improved significantly for composite materials compared to pure ones, while the Poisson's Ratio ν was not significantly changed.

Among different hyperelastic analytical models, Mooney-Rivlin two parameters was selected to predict the mechanical behaviour of PU CWPC due to the small error of 0.066 ± 0.006 with experimental data. As for rigid material of PLA CWPC, ROM was selected to verify the experimental data. ROM and Mooney-Rivlin analytical models showed statistical agreement with experimental results for the mechanical properties of PLA and PU CWPCs, respectively.

Flexible based material showed less voids content compared to rigid based material for the 3D printed samples. Voids were found to be 4.25 (±0.014) % for PU CWPC, while for PLA CWPC, they were 6.3 (±0.017) %.

Declaration of competing interest

The authors declare no competing interest.

Acknowledgement

The author would like to acknowledge the funding support of the Natural Science and Research Council (NSERC) Canada RGPIN- 2018-05899. Software used in this study was provided by CMC Microsystems.

References

[1] C. Tuloup, W. Harizi, Z. Aboura, Y. Meyer, K. Khellil, R. Lachat, On the manufacturing, integration, and wiring techniques of in situ piezoelectric devices for the manufacturing and structural health monitoring of polymer–matrix composites: A literature review, J. Intell. Mater. Syst. Struct. 30 (2019) 2351–2381. https://doi.org/10.1177/1045389X19861782.

[2] Y. Yang, G. Chiesura, B. Plovie, T. Vervust, G. Luyckx, J. Degrieck, T. Sekitani, J. Vanfleteren, Design and Integration of Flexible Sensor Matrix for in Situ Monitoring of Polymer Composites, ACS Sensors. 3 (2018) 1698–1705. https://doi.org/10.1021/acssensors.8b00425.

[3] J.B. Park, T. Okabe, N. Takeda, W.A. Curtin, Electromechanical modeling of unidirectional CFRP composites under tensile loading condition, Compos. - Part A Appl. Sci. Manuf. 33 (2002) 267–275. https://doi.org/10.1016/S1359-835X(01)00097-5.

[4] R. Balaji, M. Sasikumar, Graphene based strain and damage prediction system for polymer composites, Compos. Part A Appl. Sci. Manuf. 103 (2017) 48–59. https://doi.org/10.1016/j.compositesa.2017.09.006.

[5] R. Balaji, M. Sasikumar, Development of strain and damage monitoring system for polymer composites with embedded nickel alloys, Meas. J. Int. Meas. Confed. 111 (2017) 307–315. https://doi.org/10.1016/j.measurement.2017.07.036.

[6] J.S. Sefadi, A.S. Luyt, Morphology and properties of EVA / empty fruit bunch composites, J. Thermoplast. Compos. Mater. 25 (2012), pp.895-914. https://doi.org/10.1177/0892705711421806.

[7] R.D. Goodridge, M.L. Shofner, R.J.M. Hague, M. Mcclelland, M.R. Schlea, R.B. Johnson, C.J. Tuck, Processing of a Polyamide-12 / carbon nano fi bre composite by laser sintering,

Polym. Test. 30 (2011) 94–100. https://doi.org/10.1016/j.polymertesting.2010.10.011.

[8] N. Kumar, P.K. Jain, P. Tandon, P.M. Pandey, Additive manufacturing of flexible electrically conductive polymer composites via CNC-assisted fused layer modeling process, J. Brazilian Soc. Mech. Sci. Eng. 40 (2018). https://doi.org/10.1007/s40430-018-1116-6.

[9] M.C. Bertolini, S. Dul, G.M.O. Barra, A. Pegoretti, Poly(vinylidene fluoride)/thermoplastic polyurethane flexible and 3D printable conductive composites, J. Appl. Polym. Sci. (2020) 1–15. https://doi.org/10.1002/app.50305.

[10] V. Sankar, V. Sankar, A. Nambi, V.N. Bhat, D. Sethy, K. Balasubramaniam, S. Das, M. Guha, R. Sundara, Waterproof Flexible Polymer-Functionalized Graphene-Based Piezoresistive Strain Sensor for Structural Health Monitoring and Wearable Devices, ACS Omega. 5 (2020) 12682–12691. https://doi.org/10.1021/acsomega.9b04205.

[11] Y. Qureshi, M. Tarfaoui, K.K. Lafdi, K. Lafdi, Development of microscale flexible nylon/Ag strain sensor wire for real-time monitoring and damage detection in composite structures subjected to three-point bend test, Compos. Sci. Technol. 181 (2019) 107693. https://doi.org/10.1016/j.compscitech.2019.107693.

[12] M.A. Saleh, R. Kempers, G.W. Melenka, 3D printed continuous wire polymer composites strain sensors for structural health monitoring, Smart Mater. Struct. 28 (2019) 105041. https://doi.org/10.1088/1361-665x/aafdef.

[13] H. Nakamoto, H. Ootaka, M. Tada, I. Hirata, F. Kobayashi, F. Kojima, Stretchable Strain Sensor with Anisotropy and Application for Joint Angle Measurement, IEEE Sens. J. 16 (2016) 3572–3579. https://doi.org/10.1109/JSEN.2016.2535489.

[14] B.P. Justusson, D.M. Spagnuolo, J.H. Yu, Assessing the Applicability of Digital Image Correlation (DIC) Technique in Tensile Testing of Fabric Composites, (2013) 1–24. http://www.dtic.mil/docs/citations/ADA571047%0Apapers3://publication/doi/10.21236/ADA571047.

[15] B. Pan, K. Qian, H. Xie, A. Asundi, Two-dimensional digital image correlation for in-plane displacement and strain measurement: A review, Meas. Sci. Technol. 20 (2009). https://doi.org/10.1088/0957-0233/20/6/062001.

[16] R.H. Pritchard, P. Lava, D. Debruyne, E.M. Terentjev, Precise determination of the Poisson ratio in soft materials with 2D digital image correlation, Soft Matter. 9 (2013).

[17] Y. Ibrahim, G.W. Melenka, R. Kempers, Fabrication and tensile testing of 3D printed continuous wire polymer composites, Rapid Prototyp. J. 24 (2018) 1131–1141. https://doi.org/10.1108/RPJ-11-2017-0222.

[18] R. Matsuzaki, M. Ueda, M. Namiki, T.K. Jeong, H. Asahara, K. Horiguchi, T. Nakamura, A. Todoroki, Y. Hirano, Three-dimensional printing of continuous-fiber composites by in-nozzle impregnation, Sci. Rep. 6 (2016) 1–7. https://doi.org/10.1038/srep23058.

[19] G.W. Melenka, B.K.O. Cheung, J.S. Schofield, M.R. Dawson, J.P. Carey, Evaluation and prediction of the tensile properties of continuous fiber-reinforced 3D printed structures, Compos. Struct. 153 (2016) 866–875. https://doi.org/10.1016/j.compstruct.2016.07.018.

[20] J.F. Rodriguezjames, P.T.E. Renaud, J.F. Rodriguez, J.P. Thomas, J.E. Renaud, Characterization of the mesostructure of fused-deposition acrylonitrile-butadiene-styrene materials. Rapid Prototyp. J. (2000). https://doi.org/10.1108/13552540010337056.

[21] K. Ogi, Y. Takao, Characterization of piezoresistance behavior in a CFRP unidirectional laminate, Compos. Sci. Technol. 65 (2005) 231–239. https://doi.org/10.1016/j.compscitech.2004.07.005.

[22] G. Marckmann, E. Verron, G. Marckmann, E. Verron, Comparison of hyperelastic models for rubber-like materials, Rubber Chem. Technol. 3 (2016) 2–25. https://doi.org/10.5254/1.3547969.

[23] A. Chanda, S. Chatterjee, V. Gupta, Soft composite based hyperelastic model for anisotropic tissue characterization, J. Compos. Mater. 54 (2020) 4525–4534. https://doi.org/10.1177/0021998320935560.

[24] R. W. Ogden, G. Saccomandi, I. Sgura, Fitting hyperelastic models to experimental data, Comput. Mech. J. 34 (2004) 484-502. https://doi.org/10.1007/s00466-004-0593-y

[25] G. Sun, S. Tong, D. Chen, Z. Gong, Q. Li, Mechanical properties of hybrid composites reinforced by carbon and basalt fibers, Int. J. Mech. Sci. 148 (2018) 636–651. https://doi.org/10.1016/j.ijmecsci.2018.08.007.